Journal of Materials Science: Materials in Electronics (2019) 30:2772–2782
https://doi.org/10.1007/s10854-018-0553-4

Structural and dielectric relaxor properties of (1−*x*) $BaTiO_3$–*x*$Bi(Zn_{1/2}Zr_{1/2})O_3$ ceramics for energy storage applications

Feng Si[1] · Bin Tang[1] · Zixuan Fang[1] · Shuren Zhang[1]

Received: 8 August 2018 / Accepted: 11 December 2018 / Published online: 2 January 2019

Abstract
In this paper, the (1−*x*)$BaTiO_3$–*x*$Bi(Zn_{1/2}Zr_{1/2})O_3$ (*x* = 0.04–0.20) solid solutions were prepared using conventional solid-state reaction method. The X-ray diffraction results showed that all samples were crystalized as the perovskite structure, and there was no secondary phase in whole compositional range. For *x* = 0.04, the ceramics were in tetragonal phase, and transformed to a pesudocubic phase for $x \geq 0.08$ at ambient temperature. Temperature-dependent dielectric measurements indicated a crossover from ferroelectric behavior to relaxor-like characteristics. As the BZZ content increased, the polarization–electric field (*P*–*E*) hysteresis loops became slimmer, and the discharge energy density increased firstly, but dropped. For *x* = 0.12, the maximum discharge energy density was 0.758 J/cm^3 at 100 kV/cm, and the corresponding energy efficiency was 98%, indicating that (1−*x*)$BaTiO_3$–*x*$Bi(Zn_{1/2}Zr_{1/2})O_3$ ceramics were promising candidates for energy storage applications.

1 Introduction

With the continuous development of modern information technology, energy storage materials become increasingly important for applications, such as novel pulsed power devices, medical devices, and smart grid [1]. There are many types of energy storage components, such as conventional batteries, fuel cells, flywheels, and ceramics capacitors [2–4]. In addition, capacitors in power electronics and pulsed power system account for a signification proportion (more than 25%). More specifically, ceramic capacitors exhibit many advantages in terms of charging-discharging rate and long cycle-life. Generally, the energy storage density of dielectric materials can be defined by the following Equation:

$$U = \int EdD, \tag{1}$$

where *E* is the external electric field, *U* is the energy storage density, and *D* is the electric displacement. In order to obtain higher energy storage density, therefore, a large dielectric polarization, a low dielectric loss, and a high dielectric breakdown strength (BDS) of dielectric materials are required concurrently [5, 6]. In general, dielectric energy storage materials can be classified into four types: linear dielectrics, antiferroelectrics, ferroelectrics, and relaxor ferroelectrics. Linear dielectric including mica, glass, paraelectric ceramics and polymers show advantages in their high BDS and low energy loss, while their applications in high energy storage fields are limited by their small polarization or low dielectric constant. Ferroelectrics possess large dielectric polarization and moderate BDS, but the high dielectric loss or remnant polarization resulting in low energy density values and efficiency limits the utilization for energy storage devices [7]. Antiferroelectrics may be used for high energy storage as a result of their high dielectric polarization, small remnant polarization and moderate BDS; nevertheless, most of antiferroelectrics are Pb-based perovskite structures that is known to be harmful to the environment, such as $PbZrO_3$ [8] and $Pb_{(1-x)}La_xZr_{(1-y)}Ti_yO_3$ [9] systems. In contrast, relaxor ferroelectrics usually exhibit high dielectric polarization, low remnant polarization, and so they have promising potential for energy storage with fast discharge ability [10].

Previous studies have reported that the solid solutions of $BaTiO_3$–$BiMeO_3$ (Me = Sc, In, $Mg_{1/2}Ti_{1/2}$, $Zn_{2/3}Nb_{1/3}$, etc.) systems displayed remarkable relaxor characteristics with particular properties including relatively high dielectric constant, low dielectric loss, low temperature coefficient of capacitance at elevated temperature, and high insulation resistance in a wide range of temperature [11–13]. This

✉ Bin Tang
tangbin@uestc.edu.cn

[1] State Key Laboratory of Electronic Thin Films and Integrated Devices, University of Electronic Science and Technology of China, Chengdu 610054, China

means that the $BaTiO_3$–$BiMeO_3$ systems hold potential for high-temperature capacitors applications and high-performance energy storage applications. During the past decade $BaTiO_3$–$BiMeO_3$ systems have been extensively studied, such as $BaTiO_3$–$BiScO_3$ [14], $BaTiO_3$–$Bi(Mg_{0.5}Ti_{0.5})O_3$ [15], $BaTiO_3$–$BiInO_3$ [16], $BaTiO_3$–$Bi(Mg_{2/3}Nb_{1/3})O_3$ [17]. Recently $BaTiO_3$–$Bi(Zn_{0.5}Ti_{0.5})O_3$ ceramics have been reported to exhibit good energy density [18]. Due to the more chemical stability and higher ionic size of Zr^{4+}, the replacement of Zr^{4+} for Ti^{4+} could restrain the conduction and decrease the leakage current of $BaTiO_3$ systems. However, the energy storage properties of the $BaTiO_3$–$Bi(Zn_{1/2}Zr_{1/2})O_3$ ceramics has not yet been systematically addressed. Moreover, the $Bi(Zn_{1/2}Zr_{1/2})O_3$ compound, as one of the $BiMeO_3$ end-members, can also form stable solid solutions with $BaTiO_3$.

In this paper, we focused on the $(1-x)BaTiO_3$–$xBi(Zn_{1/2}Zr_{1/2})O_3$ ($x = 0.04$–0.20) (BT–BZZ) solid solution ceramics. Their crystal structure, dielectric properties, relaxor behavior, and energy storage properties were studied and analyzed. Moreover, excellent discharge energy density with high energy efficiency was successfully obtained.

2 Experimental procedure

A series of $(1-x)BaTiO_3$–$xBi(Zn_{1/2}Zr_{1/2})O_3$ ($x = 0.04$–0.20) ceramics were fabricated by conventional solid-state reaction route, using staring reagents: $BaCO_3$(> 99.5%), TiO_2(> 99.0%), ZnO(> 99.0%), ZrO_2(> 99.5%), Bi_2O_3(> 99.0%). The raw materials were weighed based on chemical formula and mixed in deionized water using stabilized zirconia balls as milling media for 6 h. After drying, the mixed powder was calcined in alumina crucible at 900–1000 °C for 5 h, and the parameters for growth depended on the doping content of BZZ. The calcined powder was milled again in the same way mentioned above for 6 h to obtain fine particles and dried at 110 °C. The resultant powder was granulated with polyvinyl alcohol (PVA) binder and uniaxially pressed at 20 MPa to form disks 12 mm in diameter and about 1 mm in thickness. Later, the pellets were embedded with calcined powder of the same composition to compensate for the loss of volatile Bi and then sintered at 1180–1300 °C for 2 h.

Powder X-ray diffraction (XRD) patterns were collected at ambient temperature using an X-ray diffractometer (PANalytical, Netherlands) with Cu K_α radiation ($\lambda = 0.15406$ nm) operated at 45 kV and 40 mA. Rietveld refinement of the XRD data was performed using the GSAS–EXPGUI program [19]. The microstructural observation of the samples was investigated using a scanning electron microscopy (SEM, Phenom, Netherlands). With the purpose to predict the average grains size of the BT–BZZ ceramics, the analysis of grains size distribution is performed using the "Nano Measurer" software. The density of the ceramic samples was measured by the Archimedes' method. Raman spectroscopy was carried out at ambient temperature in the range of 100–1000 cm^{-1} by a Thermo Fisher Scientific DXR (Renishaw, U.K.) with a 6 mW laser. For electrical measurements, the as-sintered ceramics were polished and coated with Ag paste, which co-fired at 800 °C for 3 min. The dielectric properties of the ceramic samples were measured from − 55 to 200 °C at 1 kHz, 10 kHz, 100 kHz, and 1 MHz using a precision LCR Meter (Agilent 4284A, U.S.A.) and an automatic temperature controller. Ferroelectric hysteresis loops were recorded under an electric field of 100 kV/cm at a frequency of 10 Hz at room temperature using a ferroelectric tester (RADIANT Precision, U.S.A.).

3 Results and discussion

Figure 1 shows the XRD patterns of $(1-x)BaTiO_3$–$xBi(Zn_{1/2}Zr_{1/2})O_3$ ($x = 0.04$–0.20) ceramics. The obtained results indicate that whole compositions show a perovskite structure without secondary phase, indicating that the solubility limit for BZZ in BT is more than 20%. When we zoom in the 2θ range of 44.6–46°, it is clear to observe the split (200) peaks for $x = 0.04$, and this finding indicates the tetragonal perovskite structure ($P4mm$), Fig. 1b. However, for $x \geq 0.08$, the sample is considered as pseudocubic structure, which can be characterized by the merging of peaks (200) and (002) into the single peak (200). This result means that the crystalline structure of samples transforms from a tetragonal structure to a pseudocubic structure. Similar phase transitions have been reported in the other systems of the $BaTiO_3$–$BiMeO_3$ ceramics [20, 21]. Moreover, with an increasing BZZ concentration, the (200) diffraction peaks shift towards lower degrees, and it indicates the changes in crystal lattice parameters and the volume of unit cell.

In order to investigate the crystallographic information of BT–BZZ ceramics further, Rietveld refinement was performed on the XRD data. For $x = 0.04$, we used the perovskite tetragonal phase (space group: $P4mm$) as the crystal model to conduct the Rietveld analysis. For $0.08 \leq x \leq 0.20$, the XRD data was refined based on the crystal model of a centro-symmetric space group $Pm\text{-}3m$. It is clear that experimental patterns and the theoretical calculation are well fitted, as shown in Fig. 2. The final R_{wp}, R_p, and γ^2 value (reliability factors) are less than 8%, 6%, and 2.4%, respectively, indicating that these refined results and structure model are reliable [22]. Table 1 lists the structural parameters of $(1-x)BaTiO_3$–$xBi(Zn_{1/2}Zr_{1/2})O_3$ ceramics obtained from Rietveld refinements. The lattice parameter (a) was found to increase with x from 4.0175 to 4.03337 for $x = 0.08$–0.12. As shown

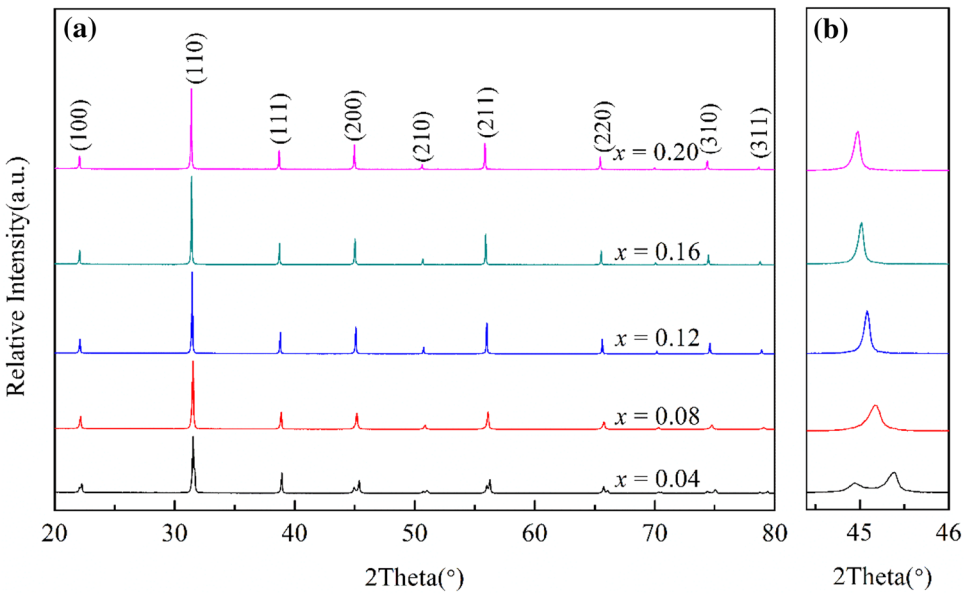

Fig. 1 XRD patterns of $(1-x)BaTiO_3$–$xBi(Zn_{1/2}Zr_{1/2})O_3$ ($x=0.04$–0.20) ceramics in the 2θ range of **a** 20–80°, **b** 44.6–46°

in Fig. 2f, cell volume increases monotonically with increasing BZZ content. According to the principles of crystal chemistry and radius-matching rule, the A-site of Ba^{2+} ions is substituted by Bi^{3+} ions, and B-site of the BT host lattice is replaced by the Zn^{2+} and Zr^{4+} ions. The radius of Bi^{3+} (1.36 Å) is smaller than that of Ba^{2+} (1.61 Å) based on coordination number of 12, while the average ionic radius of $(Zn_{0.5}Zr_{0.5})^{3+}$ (0.73 Å) is larger than that of Ti^{4+} (0.605 Å). The change in cell volume is attributable to the substitution of Ti^{4+} ions at B-site with larger size $(Zn_{0.5}Zr_{0.5})^{3+}$ ions, which suggests that the unit cell volume is dominated by the B–O_6 octahedra in the BT–BZZ perovskite structure [23].

Figure 3 illustrates the SEM micrographs of $(1-x)BaTiO_3$–$xBi(Zn_{1/2}Zr_{1/2})O_3$ ceramics sintered at the optimal temperature for 2 h. All samples present dense microstructures, and there is an evident grain growth with increasing BZZ content. The relative density of all the sample sintered at various temperature are displayed in Fig. 4. It can be observed that increasing the BZZ content could decrease the sintering temperature. Figure 5 exhibits the statistical results of the grain size distributions of $(1-x)BaTiO_3$–$xBi(Zn_{1/2}Zr_{1/2})O_3$ ceramics for different values of x. It is apparent that the average grain size increases continuously from 1.06 to 6.03 μm with increasing BZZ concentration. It is likely that the creation of oxygen vacancies resulting from sublime of Bi^{3+} element at A-site inevitably enhances the mass transportation during sintering [24–27]. The oxygen vacancies make the transfer of atoms easier than in a perfect lattice and reduced activation energy for grain growth [28], thus it improving the sintering behavior and including an increase in grain size continually [29]. In these micrographs, there is no evidence of the second phase, and this result is also in accordance with the XRD pattern.

Raman spectroscopy is an excellent technique for characterizing material structural distortions or phase transitions and probing the local structure and symmetry [30–32]. Figure 6 displays the Raman spectra of the BT–BZZ ceramics in the spectral region from 100 to 1000 cm^{-1} recorded at ambient temperature. For pure polycrystalline BT ceramics, it is usually characterized by the three phonon modes at about 270 cm^{-1} [A_1(TO)], 520 cm^{-1} [A_1(TO)] and 720 cm^{-1} [A_1(LO)] [33]. The sharp mode at 307 cm^{-1} [E(TO)] is commonly identified as a "signature" of the BT in tetragonal phase [34, 35]. For $x=0.04$, tetragonal phase structure can be characterized by the resonance dip at 180 cm^{-1} and the sharp peak at 307 cm^{-1}. For $x\geq 0.08$, the absence of these features in the spectra and a shifting and broadening of the [A_1(TO)] mode suggests the long-range ferroelectric ordering in these samples weakens and disappears [36–38]. The Raman shift of the [A_1(TO)]for $x=0.04$ is 277 cm^{-1} and for $x=0.20$ is 315 cm^{-1}. The similar phenomenon was also observed for other $BaTiO_3$–$BiMeO_3$ system (such as $BaTiO_3$–$BaAlO_3$ [39], $BaTiO_3$–$BiGdO_3$ [30]), demonstrating that the presence of lone-pair electrons from Bi^{3+} in the BT–BZZ system hardens this vibration mode, which is believed to be associated with BO_6 octahedra, particularly to the bending or of the Ti–O bonds. The phase transition from tetragonal phase to pseudocubic phase can be verified by the disappearance of the [E(TO)] mode at 307 cm^{-1}, which related to the tetragonal-pseudocubic phase transition [40–43].

The appearance of the modes at 113 cm^{-1} (labeled as 1) and 180 cm^{-1} (labeled as 2) are associated with A–O vibrations, indicating the existence of Ba^{2+} or Bi^{3+} cations enriched nano-size areas (clusters) [44, 45]. In other Bi-base perovskite modified BT ceramics [39], it can also find the

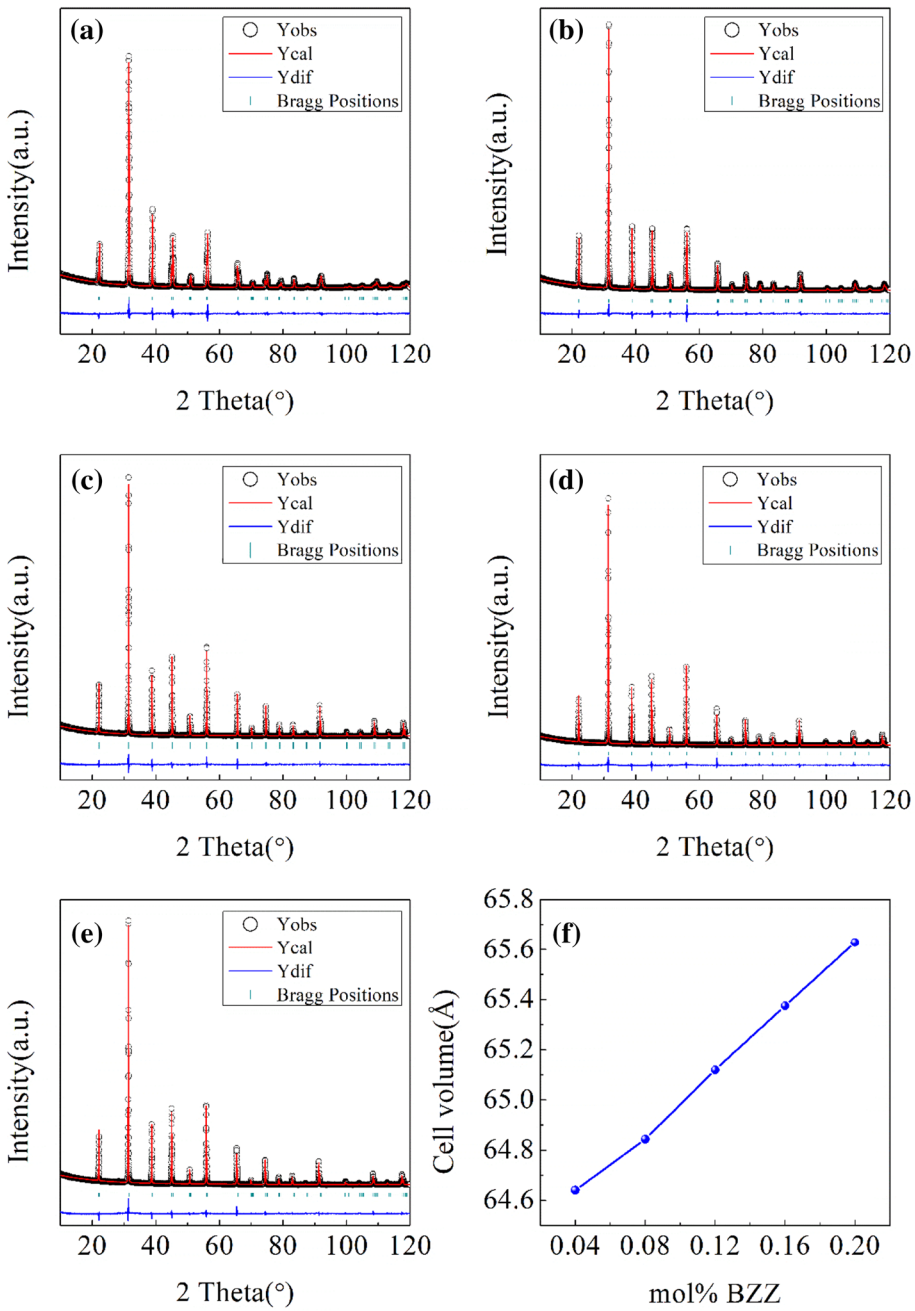

Fig. 2 Rietveld refinement plots of $(1-x)BaTiO_3$–$xBi(Zn_{1/2}Zr_{1/2})O_3$ for **a** $x=0.04$, **b** $x=0.08$, **c** $x=0.12$, **d** $x=0.16$, and **e** $x=0.20$, **f** Rietveld refined cell volume as a function of BZZ content

Table 1 Refined structural parameters for $(1-x)BaTiO_3$–$xBi(Zn_{1/2}Zr_{1/2})O_3$ ceramics obtained from Rietveld refinements

Composition	Space group	Lattice parameters (Å)	Cell volume (Å^3)	Theoretical density (g/cm^3)	R_{wp} (%)	R_p (%)	γ^2
$x=0.04$	P4mm	a = b = 4.0019 c = 4.0362	64.6406	6.096	7.22	5.49	2.36
$x=0.08$	Pm-3m	a = 4.0175	64.8437	6.182	6.80	5.10	2.20
$x=0.12$	Pm-3m	a = 4.0232	65.1201	6.260	6.40	4.87	1.87
$x=0.16$	Pm-3m	a = 4.0284	65.3729	6.339	6.90	5.24	2.05
$x=0.20$	Pm-3m	a = 4.0337	65.6313	6.417	6.59	5.08	2.16

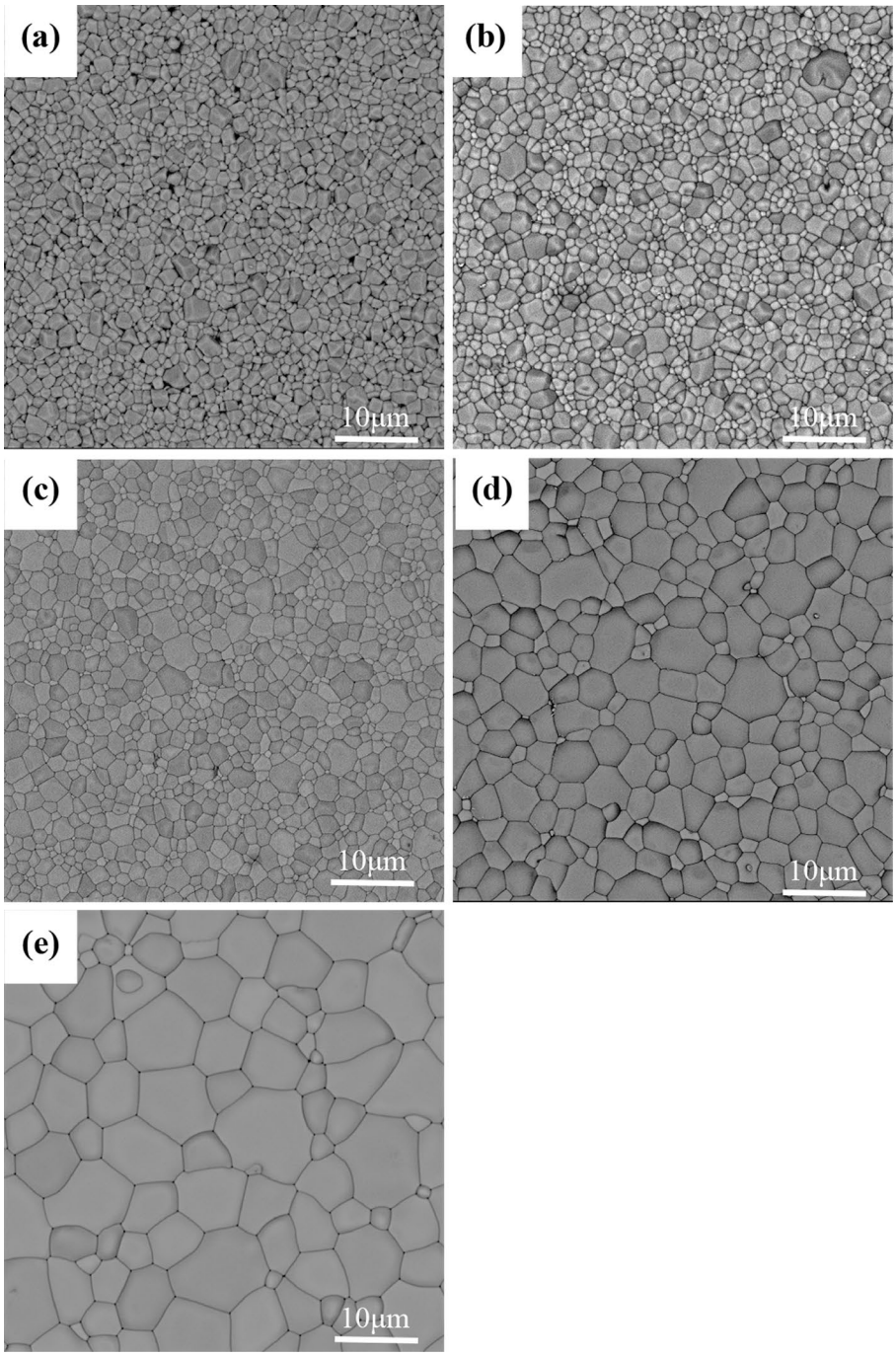

Fig. 3 SEM images of the $(1-x)BaTiO_3$–$xBi(Zn_{1/2}Zr_{1/2})O_3$ ceramics sintered at the optimal temperature for 2 h: **a** $x=0.04$, **b** $x=0.08$, **c** $x=0.12$, **d** $x=0.16$, and **e** $x=0.20$

similar spectral signatures. The broad mode at ~307 cm^{-1} shifts towards higher frequencies, which is caused by the emergence of a lone-pair of electrons from Bi^{3+} [46]. In the high-wavenumber region, the modes at 514 cm^{-1} and 718 cm^{-1} are suppressed and broadened with x value, suggesting an increase in the degree of disorder in the system [47]. Obviously, we can find an extra weak broad mode (A_{1g} octahedral breathing mode) at ~774 cm^{-1} for $x \geq 0.08$, resulting from the substitution of B-site. It is noted that an extra broad mode (A_{1g}) appears at ~774 cm^{-1} for x = 0.08. This can be assigned to the B-site substitution. The symmetrical A_{1g} mode of the BO_6 octahedra in pure or A-site doped BT became asymmetry with two or more cation occupying the B-site resulting from their different ionic radius, and thus Raman active. This finding further confirms substitution of $(Zn_{0.5}Zr_{0.5})^{3+}$ ions for Ti^{4+} ions, which will result in the local structure deformation. On the contrary, the intensity of peak at 718 cm^{-1} was found to decrease with increasing BZZ content, and it reveals a clear signature of the relaxor behavior [48].

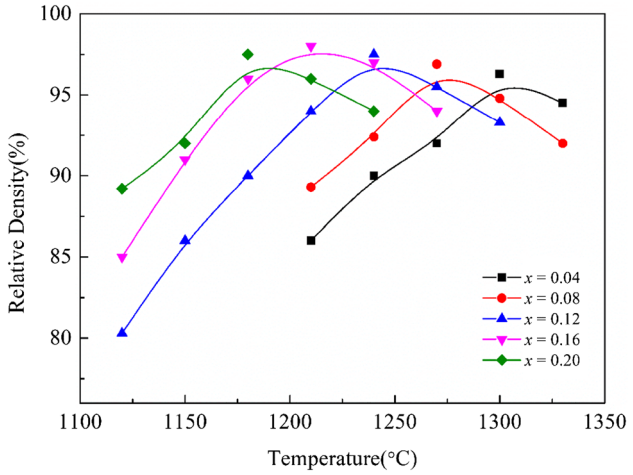

Fig. 4 Relative density of the$(1-x)BaTiO_3$–$xBi(Zn_{1/2}Zr_{1/2})O_3$ ceramics at various temperatures

Figure 7 presents the temperature dependences of dielectric constant and dielectric loss for compositions with $x = 0.04$–0.20 at various frequencies (1 kHz, 10 kHz, 100 kHz, 1 MHz). In this system, the dielectric characterization shows the crossover from ferroelectric behavior to relaxor behavior with a highly diffuse and frequency-dependent dielectric response. A dielectric peak at ~ 115 °C can be observed for $x = 0.04$, and this result is related to ferroelectric behavior. In contrast, a clear frequency dependence of the dielectric constant below the temperature of maximum permittivity (T_m) observed at $x \geq 0.08$. For example, the dielectric constant of 0.96BT–0.04BZZ ceramic at room temperature decreases from 2414 at 1 kHz to 1949 at 1 MHz. At this composition, T_m of different frequency begins to shift towards higher temperatures as the measurement frequency increases, according to the Vogel–Fulcher law [49]. The emergence of the relaxor in the BT–BZZ

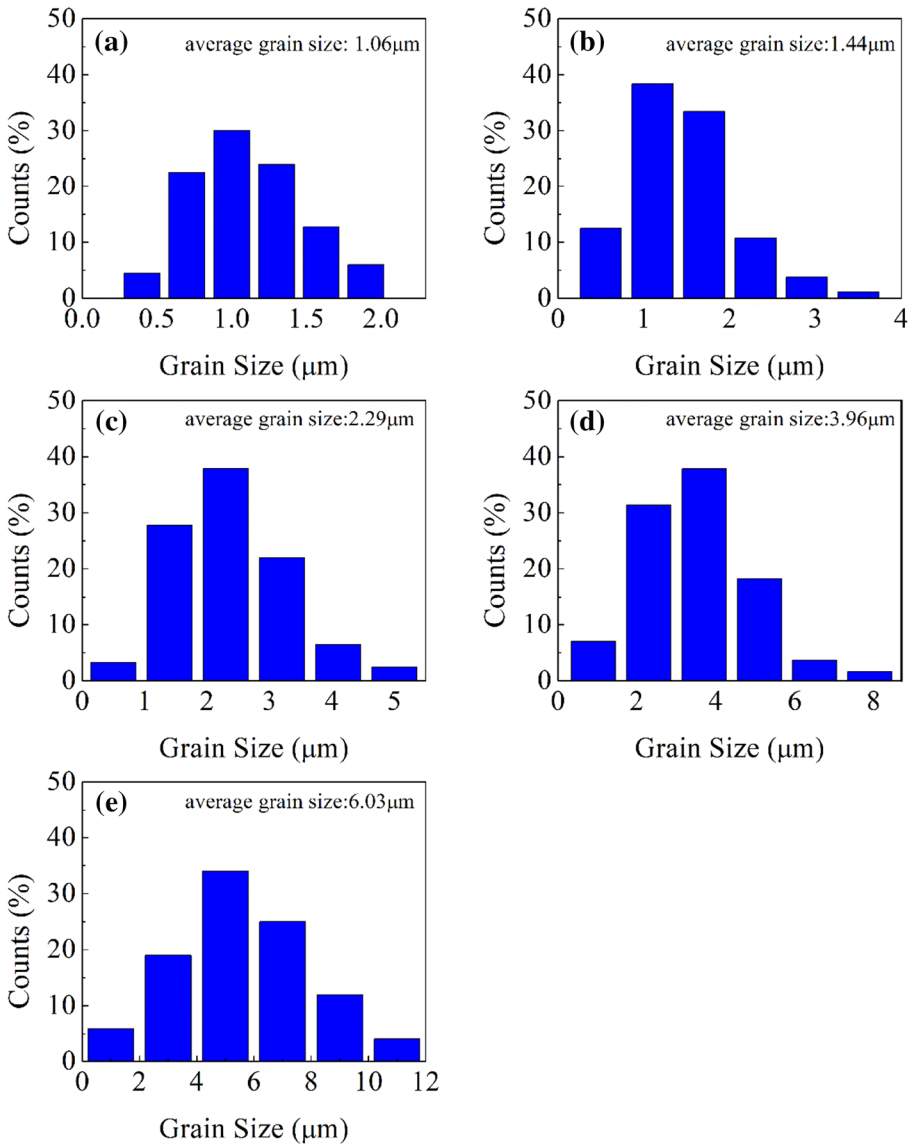

Fig. 5 Grain size distribution of the $(1-x)BaTiO_3$–$xBi(Zn_{1/2}Zr_{1/2})O_3$ ceramics: **a** $x = 0.04$, **b** $x = 0.08$, **c** $x = 0.12$, **d** $x = 0.16$, and **e** $x = 0.20$

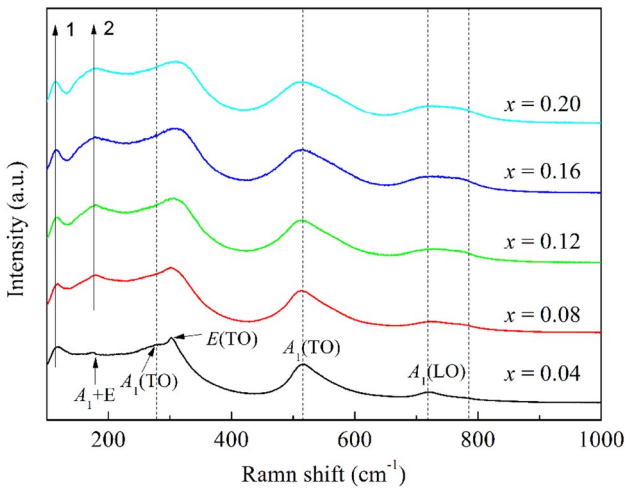

Fig. 6 Raman spectra of the$(1-x)BaTiO_3$–$xBi(Zn_{1/2}Zr_{1/2})O_3$ ceramics at room temperature

ceramics is considered to relate with heterogeneous cation substitution of Ba^{2+} by Bi^{3+} and Ti^{4+} by Zn^{2+} and Zr^{4+}, and the replacement finally increases cation disorder of crystal structure. The disorder can destroy the long-range dipolar interaction and form random fields by the differences in radius and valence state of these cations [5]. Consequently, isolated clusters of polar nano-regions(PNRs) that are only weak coupling between the adjacent clusters are formed due to random fields generated [50]. Normally, PNRs have an essential impact on relaxor behavior [51]. The variation in size and dipolar strength of PNRs and random interactions bring about a wide distribution of relaxation times leading to the dielectric peak broaden [52]. The characteristic relaxor-like behavior observed in this material system was also found in $BaTiO_3$–$BiScO_3$ [53], $BaTiO_3$–$Bi(Zn_{0.5}Ti_{0.5})O_3$ [18], $BaTiO_3$-$Bi(Mg_{0.5}Ti_{0.5})O_3$ [54] perovskites. As the BZZ content increases, this dispersive behavior becomes dominant, and it will result in flattening and broadening of the temperature-dependent permittivity. The temperature stability of dielectric materials can be effectively characterized by the temperature coefficient of permittivity (TCε) which can be estimated as follow,

$$TC\varepsilon = \frac{1}{\varepsilon}\left(\frac{\delta\varepsilon}{\delta T}\right) \tag{2}$$

The calculated results reveal that the $TC\varepsilon$ gradually increases to near-zero values for the BT–BZZ ceramics with high BZZ additives, and tolerance factor decreases monotonously with increasing BZZ concentration, as shown in Fig. 8. A lower (higher) tolerance factor is highly corresponding to a smaller (larger) $TC\varepsilon$ value, which is an

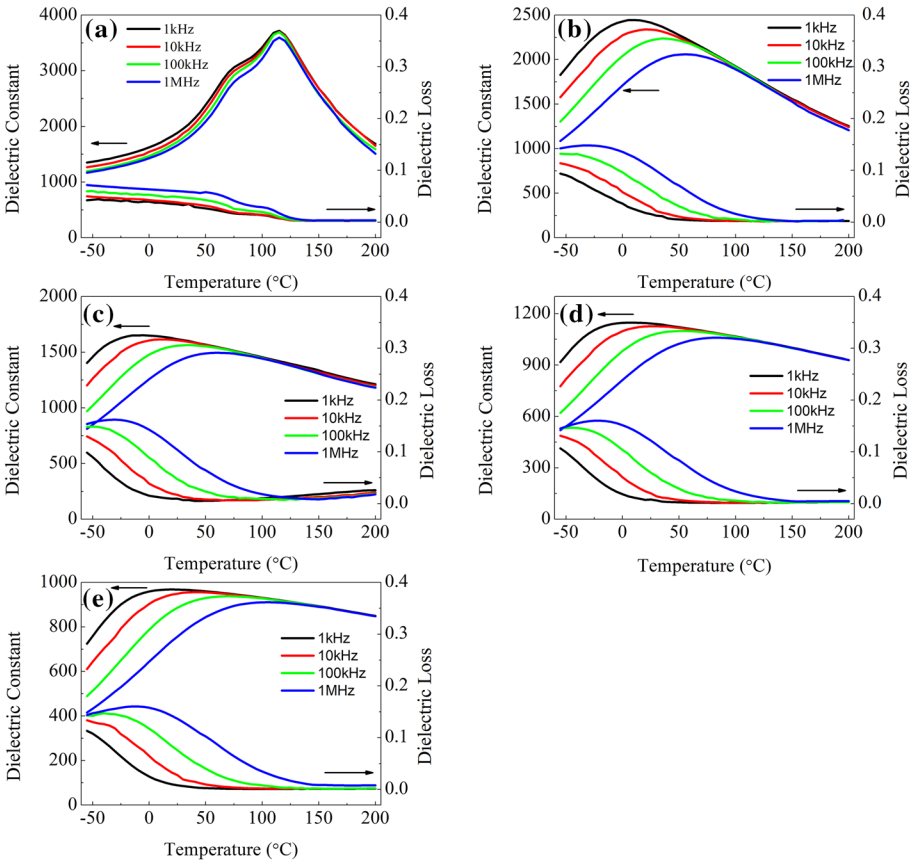

Fig. 7 Temperature dependences of dielectric constant and dielectric loss for the$(1-x)BaTiO_3$–$xBi(Zn_{1/2}Zr_{1/2})O_3$ ceramics at various frequencies: **a** $x=0.04$, **b** $x=0.08$, **c** $x=0.12$, **d** $x=0.16$, and **e** $x=0.20$

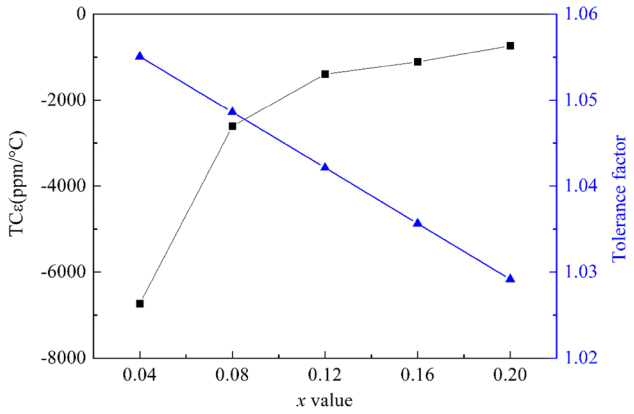

Fig. 8 Compsition dependent *TC*ε and tolerance factor

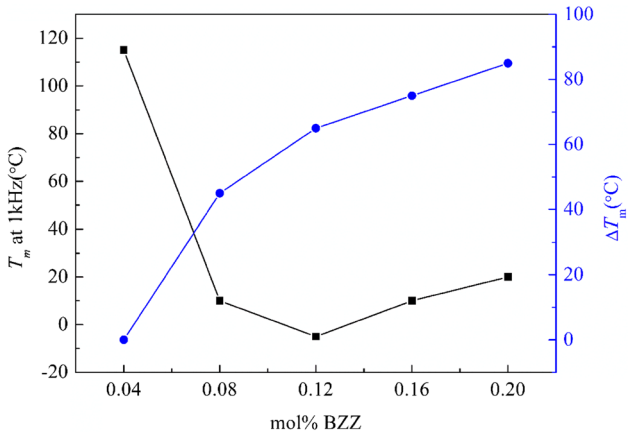

Fig. 9 T_m and ΔT_m as a function of BZZ content

empirical law to improve the temperature stability of dielectrics [55]. In other words, it is promising for the $(1-x)BaTiO_3$–$xBi(Zn_{1/2}Zr_{1/2})O_3$ ceramics with high BZZ concentrations to be utilized in such fields.

In addition, as shown in Fig. 9, T_m was found to initially drop from 115 °C (1 kHz) to -5 °C (1 kHz), but then increase upon further increase in BZZ concentration. The frequency dispersion is also evident by a parameter ΔT_m, which is calculated from Equation,

$$\Delta T_m = T_m(1MHz) - T_m(1kHz) \tag{3}$$

where T_m (1 kHz) and T_m (1 MHz) are the temperature corresponding to the maximum dielectric constant measured at 1 kHz and 1 MHz, respectively. Figure 9 shows the value of ΔT_m calculated from Eq. (3) for all samples. It is clear that ΔT_m generally increases from 0 °C to 85 °C, which also suggests the crossover from ferroelectric state to relaxor state. As is well known, the dielectric characteristics of relaxor ferroelectrics can be described by a modified Curie–Weiss law [56],

$$\frac{1}{\varepsilon} - \frac{1}{\varepsilon_m} = \frac{(T - T_m)^\gamma}{C} \tag{4}$$

where ε_m is the maximum value of the permittivity, and T_m is the corresponding temperature. C is the modified Curie–Weiss constant, and the value of γ is the degree of relaxation ranging from 1 to 2. $\gamma = 1$ corresponds to normal ferroelectric behavior, whereas $\gamma = 2$ represents ideal relaxation behavior. The plot of $\ln(1/\varepsilon\text{-}1/\varepsilon_m)$ as a function of $\ln(T\text{-}T_m)$ for the (1−x)BT–xBZZ ceramics is shown in Fig. 10. The value of γ that was obtained by fitting the permittivity data measured at 1 MHz with Eq. (4) was in the range of 1.50–1.77 with increasing x from 0.08 to 0.20, and this result manifests an obvious relaxation behavior in (1−x)BT–xBZZ ceramics.

To investigate the energy storage behaviors of the BT–BZZ ceramics, the *P*–*E* (polarization–electric field) hysteresis loops was measured. The *P*–*E* loops record at 10 Hz for all the compositions is shown in Fig. 11. In case of $x = 0.04$, we observe the well-defined ferroelectric hysteresis loop with large remnant polarization (7 μC/cm^2) and high coercive field (8.3 kV) at an applied electric field of 90 kV/cm. As x increases, however, the remnant polarization (P_r) drops rapidly and the *P*–*E* loops become slim, indicating that the long-range dipolar interaction is disturbed because of the compositional fluctuation and charge difference by the addition of BZZ. These phenomena attribute to the domain wall motion. Compared with macrodomains in ferroelectrics, the microdomains or PNRs may exist in relaxor ferroelectrics. The response of microdoamins to the applied electric field is faster than that of macrodomains because of their quite small characteristic size, which lead to slim *P*–*E* loops [10]. As mentioned above, BT–BZZ ceramics have a crossover from ferroelectric behavior to relaxor-like behavior with x increasing. Hence, slim *P*–*E* loops with small remnant polarization and coercive field can be observed when $x \geq 0.08$. There is a clear trend of decreasing of the maximum polarization (P_m) with the increase of BZZ content. These findings are linked to the incorporation of BZZ into the BT host, and the incorporation breaks the long-range dipole interaction. It can be seen that the P_r, and coercive field (E_c) also present a decline trend with the increase in x value. The low P_r and E_c is generally related to low energy loss, and it makes sense for energy storage.

The charge and discharge paths are not uniform on account of hysteresis or conduction loss. Therefore, from the practical application point of view, both the discharge energy density and energy efficiency should be considering. Commonly, the discharge energy density W_1, energy loss density W_2, and energy efficiency η can be calculated from the *P*–*E* loops as follow,

$$W_1 = \int_{P_\gamma}^{P_m} EdP \tag{5}$$

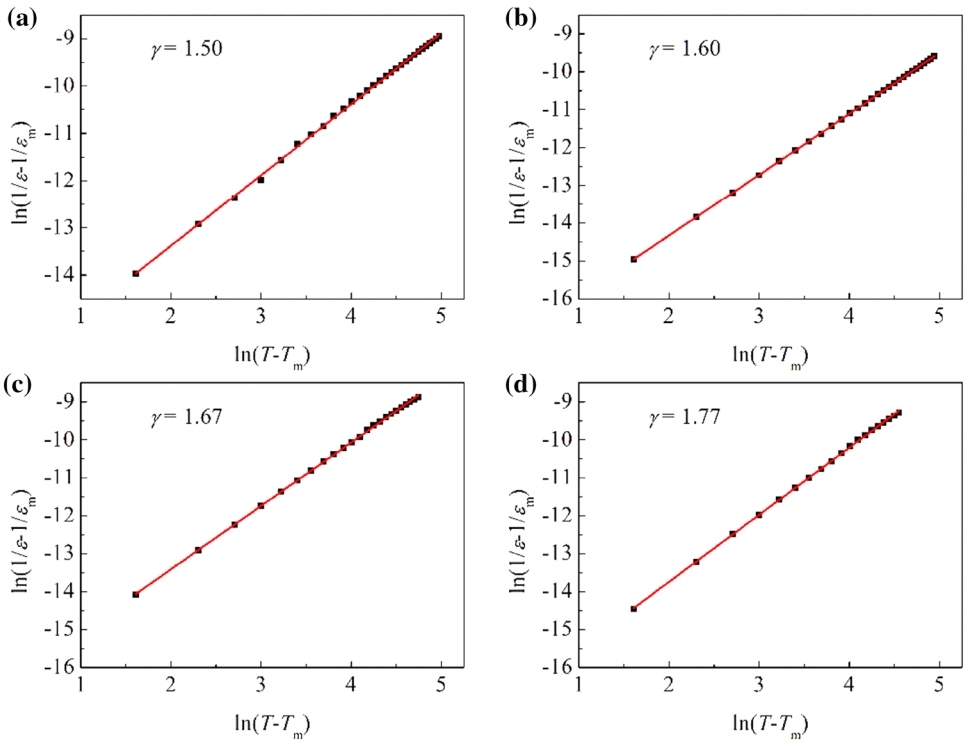

Fig. 10 Plot of $\ln(1/\varepsilon\text{-}1/\varepsilon_m)$ as a function of $\ln(T\text{-}T_m)$ for the (1−x)BT–xBZZ ceramics at the frequency of 1 MHz; **a** $x=0.08$, **b** $x=0.12$, **c** $x=0.16$, **d** $x=0.20$

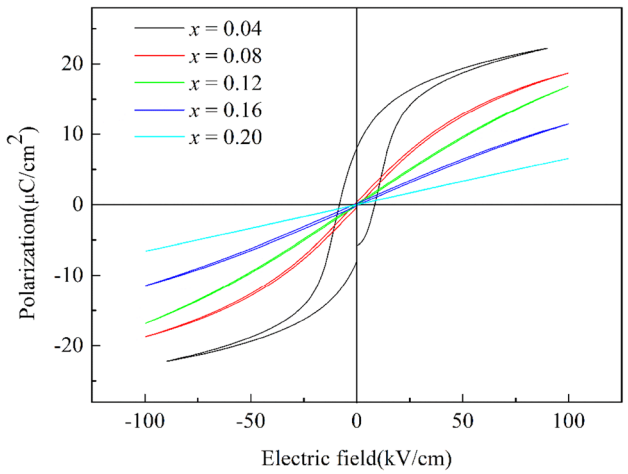

Fig. 11 P-E loops for the $(1-x)BaTiO_3$–$xBi(Zn_{1/2}Zr_{1/2})O_3$ ceramics measured at 10 Hz with a maximum applied field of 100 kV/cm

$$W_2 = \int_0^{P_m} EdP - W_1 \tag{6}$$

$$\eta = \frac{W_1}{W_1 + W_2} \times 100\% \tag{7}$$

where E and P is the applied electric field and polarization, respectively. W_2 is caused by the domain reorientation. Table 2 provides the calculated results of discharge energy density, energy loss density, and energy efficiency of the BT–BZZ ceramics. It is apparent from this table that energy efficiency of these relaxor behavior ceramics reached a high value larger than 95% at 100 kV/cm, which can be explained by the fast domain back switching resulting from their weakly coupled behaviors. The discharge energy density first increase to a maximum value at $x=0.12$ but decrease with increasing x value thereafter. On the one hand, for $x=0.04$, due to the existence of obvious ferroelectric phase with large P_r, the discharge energy density is low. On the other hand, the dielectric constant for $x=0.12$ is larger than that for $x=0.20$ at the measured temperature, thus a lower discharge energy density is observed for $x=0.20$. At last, the 0.88BT–0.12BZZ ceramic shows excellent energy storage properties: discharged energy density of 0.758 J/cm^3 and a high efficiency of 98% at 100 kV/cm. It can be expected that higher discharge energy density can be obtained at higher electric fields, if the breakdown strength

Table 2 Discharge energy density W_1, energy loss density W_2, and energy efficiency η of the $(1-x)BaTiO_3$–$xBi(Zn_{1/2}Zr_{1/2})O_3$ ceramics

	$x=0.04$	$x=0.08$	$x=0.12$	$x=0.16$	$x=0.20$
W_1 (J/cm^3)	0.383	0.700	0.758	0.523	0.321
W_2 (J/cm^3)	0.217	0.032	0.016	0.021	0.003
η (%)	63.9	95.6	98.0	96.2	99.1

is improved by further decreasing grain size, porosity and other ways.

4 Conclusions

In summary, the $(1-x)BaTiO_3$–$xBi(Zn_{1/2}Zr_{1/2})O_3$ ceramics have been successfully synthesized via the conventional solid-state reaction route. The phase structure, microstructure, dielectric properties, relaxor behavior and energy storage properties were systematically investigated. A single perovskite-type structures and dense samples were observed for all compositions. The $(1-x)BaTiO_3$–$xBi(Zn_{1/2}Zr_{1/2})O_3$ ceramics structure change from a tetragonal phase to a pesudocubic phase at room temperature. Dielectric measurement elucidated a crossover from ferroelectric behavior to frequency dispersion relaxor-like characteristics for $x \geq 0.08$, which was demonstrated by Raman studies. With an increase in the BZZ content, the temperature dependences of dielectric permittivity curve became flatter, especially for $x = 0.20$. An optimal discharge energy density of 0.758 J/cm^3 at 100 kV/cm with fairly high energy efficiency of 98% is obtained in 0.88BT–0.12BZZ ceramic, and the 0.88BT–0.12BZZ ceramic has considerable potential in energy storage applications.

Acknowledgements This work was supported by the National Natural Science Foundation of China (Grant No. 51672038).

References

1. M.H. Park, H.J. Kim, Y.J. Kim, T. Moon, K.D. Kim, C.S. Hwang, Thin $Hf_xZr_{1-x}O_2$ films: a new lead-free system for electrostatic supercapacitors with large energy storage density and robust thermal stability. Adv. Energy Mater. **4**, 14006101–14006107 (2014)
2. M.F. El-Kady, V. Strong, S. Dubin, R.B. Kaner, Laser scribing of high-performance and flexible graphene-based electrochemical capacitors. Science **335**, 1326–1330 (2012)
3. J.H. Pikul, H. Gang Zhang, J. Cho, P.V. Braun, W.P. King, High-power lithium ion microbatteries from interdigitated three-dimensional bicontinuous nanoporous electrodes. Nat. Commun. **4**, 1732–1736 (2013)
4. Z.S. Wu, K. Parvez, X. Feng, K. Mullen, Graphene-based in-plane micro-supercapacitors with high power and energy densities. Nat. Commun. **4**, 2487–2487 (2013)
5. Q. Yuan, F. Yao, Y. Wang, R. Ma, H. Wang, Relaxor ferroelectric $0.9BaTiO_3$–$0.1Bi(Zn_{0.5}Zr_{0.5})O_3$ ceramic capacitors with high energy density and temperature stable energy storage properties. J. Mater. Chem. C **5**, 9552–9558 (2017)
6. N.H. Fletcher, A.D. Hilton, B.W. Ricketts, Optimization of energy storage density in ceramic capacitors. J. Phys. D **29**, 253–258 (1996)
7. D.P. Shay, N.J. Podraza, N.J. Donnelly, C.A. Randall, D.W. Johnson, High energy density, high temperature capacitors utilizing Mn-Doped $0.8CaTiO_3$–$0.2CaHfO_3$ ceramics. J. Am. Ceram. Soc. **95**, 1348–1355 (2012)
8. T.F. Zhang, X.G. Tang, X.X. Huang, Q.X. Liu, Y.P. Jiang, Q.F. Zhou, High-temperature dielectric relaxation behaviors of relaxer-like $PbZrO_3$–$SrTiO_3$ ceramics for energy-storage applications. Energy Technol.-Ger **4**, 633–640 (2016)
9. J.F. Wang, T.Q. Yang, S.C. Chen, G. Li, High energy storage density performance of Ba, Sr-modified lead lanthanum zirconate titanate stannate antiferroelectric ceramics. Mater. Res. Bull. **48**, 3847–3849 (2013)
10. L. Jin, F. Li, S.J. Zhang, Decoding the fingerprint of ferroelectric loops: comprehension of the material properties and structures. J. Am. Ceram. Soc. **97**, 1–27 (2014)
11. Q. Hu, L. Jin, P.S. Zelenovskiy, V.Y. Shur, Y. Zhuang, Z. Xu, X. Wei, Relaxation behavior and electrical inhomogeneity in $0.9BaTiO_3$–$0.1Bi(Mg_{1/2}Ti_{1/2})O_3$ ceramic. Ceram. Int. **43**, 12828–12834 (2017)
12. L. Wu, X. Wang, L. Li, Lead-free $BaTiO_3$–$Bi(Zn_{2/3}Nb_{1/3})O_3$ weakly coupled relaxor ferroelectric materials for energy storage. RSC Adv. **6**, 14273–14282 (2016)
13. R. Muhammad, Y. Iqbal, I.M. Reaney, C. Randall, $BaTiO_3$–$Bi(Mg_{2/3}Nb_{1/3})O_3$ ceramics for high-temperature capacitor applications. J. Am. Ceram. Soc. **99**, 2089–2095 (2016)
14. H. Ogihara, C.A. Randall, S. Trolier-McKinstry, High-energy density capacitors utilizing $0.7BaTiO_3$–$0.3BiScO_3$ ceramics. J. Am. Ceram. Soc. **92**, 1719–1724 (2009)
15. P.R. Ren, X. Wang, H.Q. Fan, Y. Ren, G.Y. Zhao, Structure, relaxation behaviors and nonlinear dielectric properties of $BaTiO_3$–$Bi(Ti_{0.5}Mg_{0.5})O_3$ ceramics. Ceram. Int. **41**, 7693–7697 (2015)
16. A. Manjon-Sanz, C. Berger, M.R. Dolgos, Understanding the structure-property relationships of the ferroelectric to relaxor transition of the $(1-x)BaTiO_3$–$(x)BiInO_3$ lead-free piezoelectric system. J. Mater. Sci. **52**, 5309–5323 (2017)
17. T. Wang, L. Jin, C. Li, Q. Hu, X. Wei, D. Lupascu, Relaxor ferroelectric $BaTiO_3$–$Bi(Mg_{2/3}Nb_{1/3})O_3$ ceramics for energy storage application. J. Am. Ceram. Soc. **98**, 559–566 (2015)
18. X.B. Zhao, Z.Y. Zhou, R.H. Liang, F.H. Liu, X.L. Dong, High-energy storage performance in lead-free $(1-x)BaTiO3$–$xBi(Zn_{0.5}Ti_{0.5})O_3$ relaxor ceramics for temperature stability applications. Ceram. Int. **43**, 9060–9066 (2017)
19. B.H. Toby, EXPGUI, a graphical user interface for GSAS. J. Appl. Crystallogr. **34**, 210–213 (2001)
20. Q. Zhang, Z.R. Li, F. Li, Z. Xu, Structural and dielectric properties of Bi $(Mg_{1/2}Ti_{1/2})O_3$–$BaTiO_3$ lead-free ceramics. J. Am. Ceram. Soc. **94**, 4335–4339 (2011)
21. X.C. Huang, H. Hao, S.J. Zhang, H.X. Liu, W.Q. Zhang, Q. Xu, M.H. Cao, Structure and dielectric properties of $BaTiO_3$–$BiYO_3$ perovskite solid solutions. J. Am. Ceram. Soc. **97**, 1797–1801 (2014)
22. M. Ferrari, L. Lutterotti, Method for the simultaneous determination of anisotropic residual-stresses and texture by X-ray-diffraction. J. Appl. Phys. **76**, 7246–7255 (1994)
23. Z.B. Shen, X.H. Wang, B.C. Luo, L.T. Li, $BaTiO_3$–$BiYbO_3$ perovskite materials for energy storage applications. J. Mater. Chem. A **3**, 18146–18153 (2015)
24. N. Kumar, E.A. Patterson, T. Fromling, E.P. Gorzkowski, P. Eschbach, I. Love, M.P. Muller, R.A. De Souza, J. Tucker, S.R. Reese, D.P. Cann, Defect mechanisms in $BaTiO_3$–$BiMO_3$ ceramics. J. Am. Ceram. Soc. **101**, 2376–2390 (2018)
25. H.B. Yang, F. Yan, Y. Lin, T. Wang, Novel strontium titanate-based lead-free ceramics for high-energy storage applications. ACS Sustain. Chem. Eng. **5**, 10215–10222 (2017)
26. F. Rubio-Marcos, P. Marchet, X. Vendrell, J.J. Romero, F. Rémondière, L. Mestres, J.F. Fernández, Effect of MnO doping on the structure, microstructure and electrical properties of

the (K,Na,Li)(Nb,Ta,Sb)O_3 lead-free piezoceramics. J. Alloys Compd. **509**, 8804–8811 (2011)
27. M. Zhu, L. Liu, Y. Hou, H. Wang, H. Yan, Microstructure and electrical properties of MnO-doped $(Na_{0.5}Bi_{0.5})_{0.92}Ba_{0.08}TiO_3$ lead-free piezoceramics. J. Am. Ceram. Soc. **90**, 120–124 (2007)
28. S. Shukla, S. Seal, R. Vij, S. Bandyopadhyay, Reduced activation energy for grain growth in nanocrystalline yttria-stabilized zirconia. Nano Lett. **3**, 397–401 (2003)
29. M.K. Zhu, L.Y. Liu, Y.D. Hou, H. Wang, H. Yan, Microstructure and electrical properties of MnO-doped (Na0.5Bi0.5)(0.92) Ba0.08TiO_3 lead-free piezoceramics. J. Am. Ceram. Soc. **90**, 120–124 (2007)
30. G. Schileo, A. Feteira, K. Reichmann, M. Li, D.C. Sinclair, Structure–property relationships in (1−x)$BaTiO_3$–x$BiGdO_3$ ceramics. J. Eur. Ceram. Soc. **35**, 2479–2488 (2015)
31. Z. Xiong, B. Tang, C. Yang, S. Zhang, Correlation between structures and microwave dielectric properties of Ba3.75Nd9.5–xSmxTi17.5(Cr1/2Nb1/2)0.5O54 ceramics. J. Alloys Compd. **740**, 492–499 (2018)
32. Z. Xiong, B. Tang, Z. Fang, C. Yang, S. Zhang, Effects of (Cr0.5Ta0.5)4+ on structure and microwave dielectric properties of Ca0.61Nd0.26TiO_3 ceramics. Ceram. Int. **44**, 7771–7779 (2018)
33. J. Pokorny, U.M. Pasha, L. Ben, O.P. Thakur, D.C. Sinclair, I.M. Reaney, Use of Raman spectroscopy to determine the site occupancy of dopants in $BaTiO_3$. J. Appl. Phys. **109**, 1141101–1141105 (2011)
34. U.D. Venkateswaran, V.M. Naik, R. Naik, High-pressure Raman studies of polycrystalline $BaTiO_3$. Phys. Rev. B **58**, 14256–14260 (1998)
35. P.R. Ren, H.Q. Fan, X. Wang, G.Z. Dong, Phase transition, high figure of merit and polar nano-regions in dielectric tunable lanthanum substituted barium titanate. J. Alloys Compd. **617**, 337–344 (2014)
36. N. Baskaran, A. Ghule, C. Bhongale, R. Murugan, H. Chang, Phase transformation studies of ceramic $BaTiO_3$ using thermo-Raman and dielectric constant measurements. J. Appl. Phys. **91**, 10038–10043 (2002)
37. N.K. Karan, R.S. Katiyar, T. Maiti, R. Guo, A.S. Bhalla, Raman spectral studies of Zr^{4+}-rich $BaZr_xTi_{1-x}O_3$(0.5â©½xâ©½1.00) phase diagram. J. Raman Spectrosc. **40**, 370–375 (2009)
38. U.M. Pasha, H. Zheng, O.P. Thakur, A. Feteira, K.R. Whittle, D.C. Sinclair, I.M. Reaney, In situ Raman spectroscopy of A-site doped barium titanate. Appl. Phys. Lett. **91**, 0629081–0629083 (2007)
39. S.Y. Zheng, E. Odendo, L.J. Liu, D.P. Shi, Y.M. Huang, L.L. Fan, J. Chen, L. Fang, B. Elouadi, Electrostrictive and relaxor ferroelectric behavior in $BiAlO_3$-modified $BaTiO_3$ lead-free ceramics. J. Appl. Phys. **113**, 0941021–0941025 (2013)
40. Z.H. Yao, H.X. Liu, Y. Liu, Z.H. Wu, Z.Y. Shen, Y. Liu, M.H. Cao, Structure and dielectric behavior of Nd-doped $BaTiO_3$ perovskites. Mater. Chem. Phys. **109**, 475–481 (2008)
41. P.S. Dobal, A. Dixit, R.S. Katiyar, Z. Yu, R. Guo, A.S. Bhalla, Micro-Raman scattering and dielectric investigations of phase transition behavior in the $BaTiO_3$–$BaZrO_3$ system. J. Appl. Phys. **89**, 8085–8091 (2001)
42. P.S. Dobal, A. Dixit, R.S. Katiyar, Effect of lanthanum substitution on the Raman spectra of barium titanate thin films. J. Raman Spectrosc. **38**, 142–146 (2007)
43. H. Hayashi, T. Nakamura, T. Ebina, In-situ Raman spectroscopy of $BaTiO_3$ particles for tetragonal-cubic transformation. J. Phys. Chem. Solids **74**, 957–962 (2013)
44. J. Kreisel, P. Bouvier, M. Maglione, B. Dkhil, A. Simon, High-pressure Raman investigation of the Pb-free relaxor $BaTi_{0.65}Zr_{0.35}O_3$. Phys. Rev. B **69**, 0921041–0921044 (2004)
45. X. Chen, J. Chen, D. Ma, L. Fang, H. Zhou, High relative permittivity, low dielectric loss and good thermal stability of $BaTiO_3$-Bi(Mg0.5$Zr_{0.5}$)O_3 solid solution. Ceram. Int. **41**, 2081–2088 (2015)
46. T. Strathdee, L. Luisman, A. Feteira, K. Reichmann, F. Morrison, Ferroelectric-to-Relaxor Crossover in (1-x)$BaTiO_3$-x$BiYbO_3$ ($0 \leq x \leq 0.08$) Ceramics. J. Am. Ceram. Soc. **94**, 2292–2295 (2011)
47. X. Chen, J. Chen, G. Huang, D. Ma, L. Fang, H. Zhou, Relaxor Behavior and Dielectric Properties of Bi($Zn_{2/3}Nb_{1/3}$)O_3-Modified $BaTiO_3$ Ceramics. J. Electron. Mater. **44**, 4804–4810 (2015)
48. R. Farhi, M. El Marssi, A. Simon, J. Ravez, A Raman and dielectric study of ferroelectric ceramics. Eur. Phys. J. B **9**, 599–604 (1999)
49. L.E. Cross, Relaxor ferroelectrics. Ferroelectrics **76**, 241–267 (1987)
50. N. Triamnak, R. Yimnirun, J. Pokorny, D.P. Cann, D.C. Lupascu, Relaxor Characteristics of the Phase Transformation in (1 – x) $BaTiO_3$–x$Bi(Zn_{1/2}Ti_{1/2})O_3$ Perovskite Ceramics. J. Am. Ceram. Soc. **96**, 3176–3182 (2013)
51. G.A. Samara, The relaxational properties of compositionally disordered ABO_3 perovskites. J. Phys.-Condens. Matter **15**, R367–R411 (2003)
52. N. Kumar, A. Ionin, T. Ansell, S. Kwon, W. Hackenberger, D. Cann, Multilayer ceramic capacitors based on relaxor $BaTiO_3$–$Bi(Zn_{1/2}Ti_{1/2})O_3$ for temperature stable and high energy density capacitor applications. Appl. Phys. Lett. **106**, 2529011–2529014 (2015)
53. H. Ogihara, C.A. Randall, S. Trolier-McKinstry, Weakly coupled relaxor behavior of $BaTiO_3$–$BiScO_3$ ceramics. J. Am. Ceram. Soc. **92**, 110–118 (2009)
54. D.H. Choi, A. Baker, M. Lanagan, S. Trolier-McKinstry, C. Randall, D. Johnson, Structural and dielectric properties in (1−x) $BaTiO_3$–x$Bi(Mg_{1/2}Ti_{1/2})O_3$Ceramics ($0.1 \leq x \leq 0.5$) and potential for high-voltage multilayer capacitors. J. Am. Ceram. Soc. **96**, 2197–2202 (2013)
55. N. Raengthon, C. McCue, D.P. Cann, Relationship between tolerance factor and temperature coefficient of permittivity of temperature-stable high permittivity BaTiO3–$Bi(Me)O_3$ compounds, J. Adv. Dielectr. **6**, 1650002 (2016)
56. I.A. Santos, J.A. Eiras, Phenomenological description of the diffuse phase transition in ferroelectrics. J Phys-Condens Mat **13**, 11733–11740 (2001)